



RESEARCH ARTICLE

Nature-inspired 3D hierarchical carbon nanotube matrices enable extraordinary solar steam generation

Chuanshuai Dong¹  | Lei Chen¹ | Weiquan Lin¹ | Zipai Li¹ | Linjie Wei¹ |
Chaohua Peng¹ | Huan Liu¹ | Ronghui Qi¹ | Lin Lu²  | Lizhi Zhang^{1,3}

¹Key Laboratory of Enhanced Heat Transfer and Energy Conservation of Education Ministry, School of Chemistry and Chemical Engineering, South China University of Technology, Guangzhou, China

²Department of Building Environment and Energy Engineering, The Hong Kong Polytechnic University, Hong Kong, China

³State Key Laboratory of Subtropical Building and Urban Science, South China University of Technology, Guangzhou, China

Correspondence

Chuanshuai Dong and Lizhi Zhang, Key Laboratory of Enhanced Heat Transfer and Energy Conservation of Education Ministry, School of Chemistry and Chemical Engineering, South China University of Technology, Guangzhou 510640, China.

Email: dongcs@scut.edu.cn and Lzzhang@scut.edu.cn

Funding information

National Natural Science Foundation of China, Grant/Award Numbers: 52476072, 51936005; Young Talent Support Project of Guangzhou Association for Science and Technology

Abstract

Interfacial solar evaporation, which captures solar energy and localizes the absorbed heat for water evaporation, is considered a promising technology for seawater desalination and solar energy conversion. However, it is currently limited by its low photothermal conversion efficiency, salt accumulation, and poor reliability. Herein, inspired by human intestinal villi structure, we design and fabricate a novel intestinal villi-like nitrogen-doped carbon nanotubes solar steam generator (N-CNTs SSG) consisting of three-dimensional (3D) hierarchical carbon nanotube matrices for ultrahigh solar evaporation efficiency. The 3D matrices with radial direction nitrogen-doped carbon nanotube clusters achieve ultrahigh surface area, photothermal efficiency, and hydrophilicity, which significantly intensifies the whole interfacial solar evaporation process. The new solar evaporation efficiency reaches as high as 96.8%. Furthermore, our ab initio molecular dynamics simulation reveals that N-doped carbon nanotubes exhibit a greater number of electronic states in close proximity to the Fermi level when compared to pristine carbon nanotubes. The outstanding absorptivity in the full solar spectrum and high solar altitude angles of the 3D hierarchical carbon nanotube matrices offer great potential to enable ultrahigh photothermal conversion under all-day and all-season circumstances.

KEYWORDS

fermi level, interfacial solar evaporation, nitrogen-doped carbon nanotubes, photothermal conversion

Chuanshuai Dong and Lei Chen contributed equally to this study.

This is an open access article under the terms of the [Creative Commons Attribution](https://creativecommons.org/licenses/by/4.0/) License, which permits use, distribution and reproduction in any medium, provided the original work is properly cited.

© 2025 The Author(s). *Carbon Energy* published by Wenzhou University and John Wiley & Sons Australia, Ltd.

1 | INTRODUCTION

Taking full utilization of solar energy for clean water production is the ultimate path to solving the water and energy crises.^{1,2} Solar steam generation appeared in recent years and is considered a promising technology for sunlight-driven water production through harvesting solar light and further converting solar energy into steam on the air-water interface by photothermal materials.³ Instead of heating the bulk liquid, interfacial heating and evaporation in a solar steam generator enable low heat loss and high solar evaporation efficiency. The evaporation procedure is mainly governed by three steps, namely water transportation,^{4–8} phase transition,^{9–11} and vapor diffusion.^{12–14}

As the core component of the solar steam generation system, the desirable evaporator is expected to achieve excellent hydrophilicity for continuous water transportation, broadband absorbency for high photothermal conversion efficiency, porous structure for vapor to escape, and anti-fouling of salt for long service life.^{15,16} As for water transportation, wood enables a high water transportation efficiency from roots to leaves through highly oriented tracheids and vessel tissues.^{17–19} Thus, wood-based solar steam generators demonstrated huge potential due to their good hydrophilicity, lightweight structure, inherent microchannels for water transportation, thermal insulation, and low cost.^{20–23} Thirteen natural woods, including hard and soft woods, were examined comprehensively in solar steam generation, and the solar evaporation efficiency ranged from 46.8% to 86.7%.²⁴ In addition, Li's research group performed a comprehensive investigation on solar steam generation and adopted the directional channels to achieve long-term high evaporation efficiency.^{25–28}

Generally, the solar steam evaporator is designed to be optically thin and coated by a high-absorptivity layer, such as graphite,^{29,30} graphene oxide,^{31,32} plasmonic nanoparticles,^{33,34} metal oxides,^{35,36} and carbon nanotubes (CNTs).^{33,37} However, the feature of only the top surface working may result in several problems, such as (1) the inevitable heat loss by heat radiation and convection from the high-temperature top surface, (2) the reduction in the photothermal conversion efficiency induced by the diffuse reflections at the top surface, and (3) the insufficient evaporation sites or area at the top surface.^{38–44} In addition, the recent investigation indicated that a deeper "interface zone" would result in a higher evaporation efficiency.⁴⁵ However, conventional porous evaporators are faced with a large number of dead pores, where the vapor might stagnate.^{46–49} Thus, the challenge remains on how to develop a solar steam evaporator to achieve a full-domain photothermal conversion and water

evaporation as well as substantial pathways for vapor to escape. The human intestinal villi is a unique structural and functional unit for luminal sensing, digestion, absorption, secretion, and immune defense in the small intestine.^{50,51} Subepithelial fibroblasts form a 3D cellular network in the villi. One of the key functions of villi structure is to significantly increase the specific area. As the contact area also plays an important role in solar steam generators, inspired by villi structure, we develop a novel nitrogen (N)-doped carbon nanotubes solar steam generator (N-CNTs SSG) through in situ growing of CNT matrices on the internal surface of the vertically aligned microscopic channels. The 3D hierarchical CNT matrices enabled a full-domain photothermal conversion in the vertically aligned channels with a full solar spectrum, as shown in Figure 1. Our ab initio molecular dynamics (AIMD) simulations reveal that N-CNTs exhibit a greater number of electronic states in close proximity to the Fermi level, which expands the range of wavelengths absorbed by solar radiation and facilitates efficient optical transitions. The intestinal villi-like N-CNTs matrices grow densely on the channel surface with melamine as the carbon source and cobalt oxide as the catalyst. The synergistic effect of multi-reflection, diffuse reflection, and reabsorption in the intestinal villi-like N-CNTs matrices decorated channels achieves an ultrahigh absorbency of over 98.5% for the full solar spectrum. Furthermore, the 3D hierarchical porous structure by the intestinal villi-like N-CNTs and vertically aligned channels enables excellent superhydrophilicity and huge specific surface area. The contact angle is significantly reduced to around 0° and the specific surface area is improved to 184.4%. Furthermore, the extremely low thermal conductivity of the amorphous carbon skeleton effectively prevents heat loss from the localized heating surface to the bulk water. Based on the outstanding full-domain photothermal conversion efficiency, water transportation ability, and extraordinary thermal insulation property, the novel intestinal villi-like N-CNTs SSG exhibits a net solar-evaporation efficiency of 96.8% under one sun illumination. The novel intestinal villi-like N-CNTs SSG demonstrates great potential in addressing the worldwide water crisis.

2 | RESULTS

2.1 | Fabrication and characterization of intestinal villi-like 3D N-CNTs matrices

Since a general solar evaporation process is mainly governed by three steps, namely water transportation, phase transition, and vapor diffusion, we designed and fabricated a novel

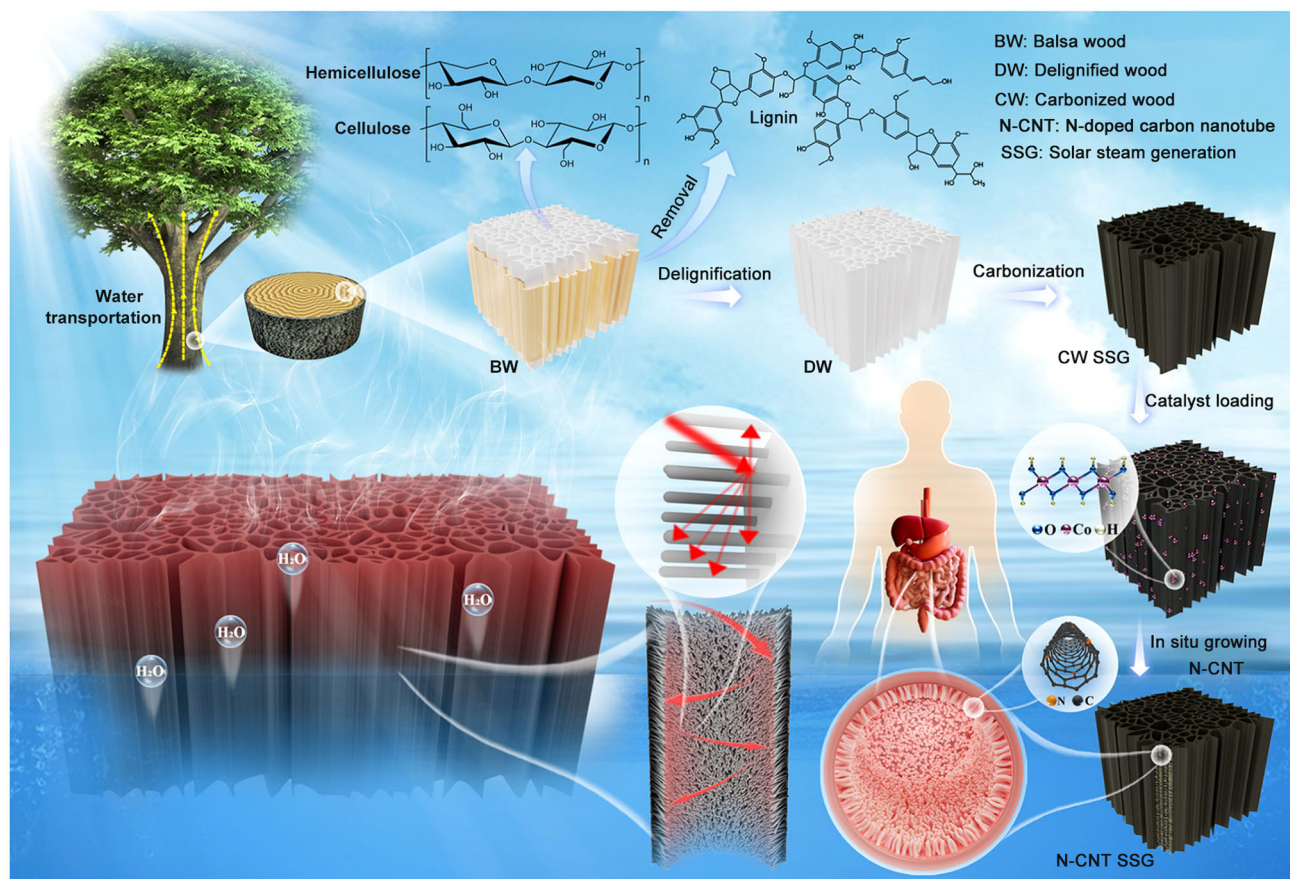


FIGURE 1 Schematic illustration of the fabrication process for the intestinal villi-like N-CNTs SSG.

intestinal villi-like N-CNTs SSG consisting of 3D hierarchical CNT matrices, inspired by the function of intestinal villi. Compared with conventional SSGs, the 3D hierarchical structure of the in-situ N-CNTs facilitates ultrahigh photothermal conversion efficiency for the full solar spectrum in the vertically aligned channels.

The 3D hierarchical structure harnessing in-situ N-CNTs was developed via thermal-chemical vapor deposition (T-CVD) technology (more details in Section 4). Due to its lightweight structure and inherent microchannels for water transportation, biomass wood was selected as the basic material. To pick out the most optimized wood-based 3D structure, typical wood materials, including poplar wood, paulownia wood, linden wood, white oak wood, pine wood, pear wood, and balsa wood, were used and compared. The microstructures of these carbonized woods are illustrated in Figure S1 (top view) and Figure S2 (cross-sectional view). Considering the vertically aligned microchannels, interconnected pore networks, and densities (Figure S3), balsa wood was selected. As illustrated in Figure 1, the biomass wood is converted into a porous structure with vertically aligned channels through delignification and carbonization processes. Scanning electron microscopy (SEM) images show the preservation of hierarchically

porous structures with highly orientated open channels in carbon wood (CW) after carbonization (Figure 2A). Then, the intestinal villi-like N-CNT fibers grow in situ on the vertically aligned channels via T-CVD technology at 700°C (Figure S4). Normally, the light absorption ability of CNTs is closely related to the graphitization degree, which mainly depends on the catalyst temperature. However, the excessively high temperature might lead to the collapse of the wood structure, which would destroy the vertically aligned microscopic channels. To keep the stability of the wood-based skeleton, the catalyst temperature was selected as 700°C, which might sacrifice the graphitization of CNTs to some extent. To ensure excellent photothermal conversion efficiency, N-doping is necessary. Actually, the N-doping of CNTs was intrinsically achieved during the in-situ growing process without extra treatment and materials. The mechanism for the in-situ growth of N-CNTs matrices on the channel surface is that the cobalt hydroxide ($\text{Co}(\text{OH})_2$) dehydrated at 700°C to produce cobalt oxide as catalysts for subsequent reaction with melamine to form the encapsulated cobalt oxide nanoparticles within the N-CNTs on carbonized wood (N-CNT/CW). The T-CVD strategy provides a simple and rapid strategy to prepare large-area N-CNTs materials.

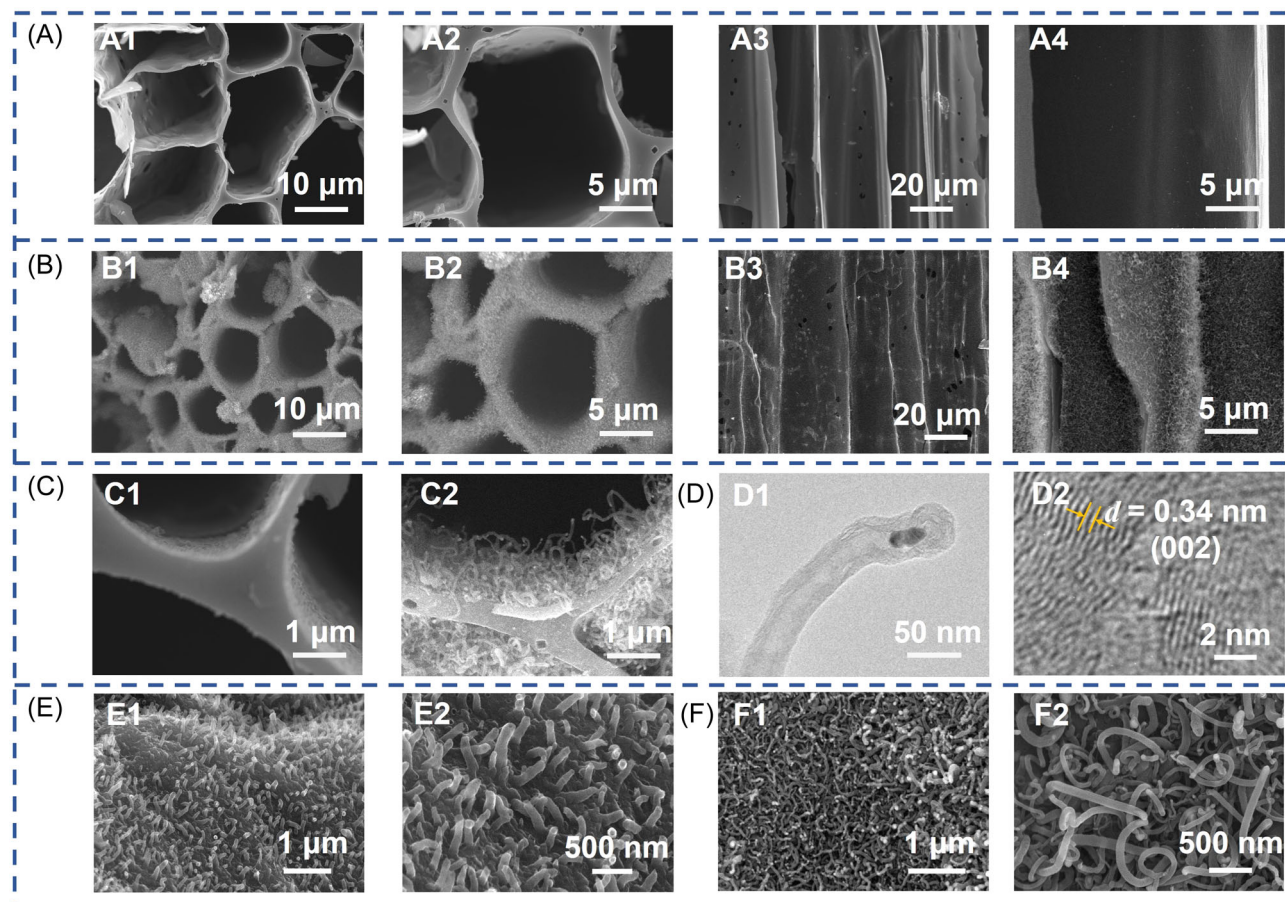


FIGURE 2 Structural and morphological characterizations. (A) SEM of the conventional CW SSG; (B) SEM image of the intestinal villi-like N-CNTs SSG, top view and cross-sectional view; (C) comparison of the microscopic structure between CW SSG and intestinal villi-like N-CNTs SSG; (D) TEM and HRTEM image of the N-CNTs; (E, F) SEM images of the N-CNTs matrices without and with NaOH solution.

The SEM images of the N-CNTs SSG confirm a full coverage of N-CNTs matrices on each vertically aligned channel of the CW structure, as shown in Figure 2B (top view and cross-sectional views). Obviously, the interlaced N-CNTs matrices, with a length of 1–2 μm and diameter of 50–100 nm, grow uniformly in the interior surface of the channels. Compared with conventional CW structure (Figure 2A), the orientated microchannels are well-retained and further equipped by the N-CNTs (Figure S5), providing a 3D hierarchical structure. A loose N-CNTs network layer composed of various bending CNTs grows locally on the interior surface, significantly improving the specific surface area, evaporation sites, and water-lifting ability (Figure 2C). Furthermore, the high-resolution transmission electron microscopy (HRTEM) images (Figure 2D) demonstrate that the cobalt hydroxide particle is encapsulated in the N-CNTs matrices, with a typical bamboo-like structure, ascribing a typical tip-growth dissolution-extrusion mechanism.⁵² The highly crystalline graphitic carbon becomes the

coating layer, and the lattice spacing of 0.34 nm is considered to be the (002) plane of graphitic carbon. Furthermore, the results of energy dispersive spectroscopy (EDS) tests (Figures S6 and S7) prove that N atoms are uniformly doped into the CNT skeleton, and a comparison of the mapping diagrams of the elements O and Co reveals a certain degree of O build-up at the position of Co, which proves the presence of cobalt oxides. The quantitative element distribution is presented in Table S1.

To investigate the effect of catalysts on the growth process of CNT matrices, CW SSGs, with and without the addition of NaOH solution, were prepared after they were immersed in $\text{Co}(\text{NO}_3)_2$ solution, and then heated with melamine in a tube furnace. Figure 2E,F presents the morphologies of N-CNTs matrices with and without NaOH solution. Without NaOH solution treatment, the N-CNTs matrices turn more vertical but too sparse and dwarfish, like vertical silkworms. This is mainly attributed to the oxygen produced during the decomposition of cobalt nitrate by heating, which oxidizes the

decomposition product, cobalt oxide, resulting in poorer performance in growing CNTs. Once the catalyst is confirmed, the length and compactness of N-CNTs clusters are mainly controlled by varying the growth time. The morphologies of N-CNTs matrices with different growth times are demonstrated in Figure 2B (120 min), Figure S8, and Figure S9 (60, 90, and 150 min), respectively. Obviously, very sparse and low N-CNTs matrices grow on the surface at 60 and 90 min due to insufficient growth time. When the growth time approaches 120 min, a dense N-CNTs clusters could be obtained.

Typically, the defective (D band) and graphitic (G band) signals located at 1350 and 1582 cm^{-1} are observed in the Raman spectra. The corresponding intensity ratio (I_D/I_G) can be used to reveal the degree of graphitization

of carbon materials. Figure 3A demonstrates the reduction of the intensity ratio (I_D/I_G) from 3.08 of CW SSG to 2.34 of N-CNTs SSG after in-situ growth of CNTs, proving the increased graphitization of the material. The chemical composition of N-CNT SSG is verified by X-ray diffraction (XRD) and X-ray photoelectron spectroscopy (XPS). As shown in Figure 3B, the peaks at 27.6° and 44.3° can correspond well to the (002) and (100) crystal planes of graphitic carbon, and the peaks at 34.0° , 40.2° , and 68.6° can correspond to the (111), (002), and (311) crystal facets of CoO, respectively (PDF#42-1300). The corresponding XPS spectra of the N-CNT SSG are shown in Figure 3C,D. The high-resolution C 1s spectrum can be fitted to four peaks at 284.5, 285.6, 287.2, and 290.1 eV, corresponding to the C-C, C-N, C-O, and O=C-O species, respectively. The high-resolution N 1s spectrum

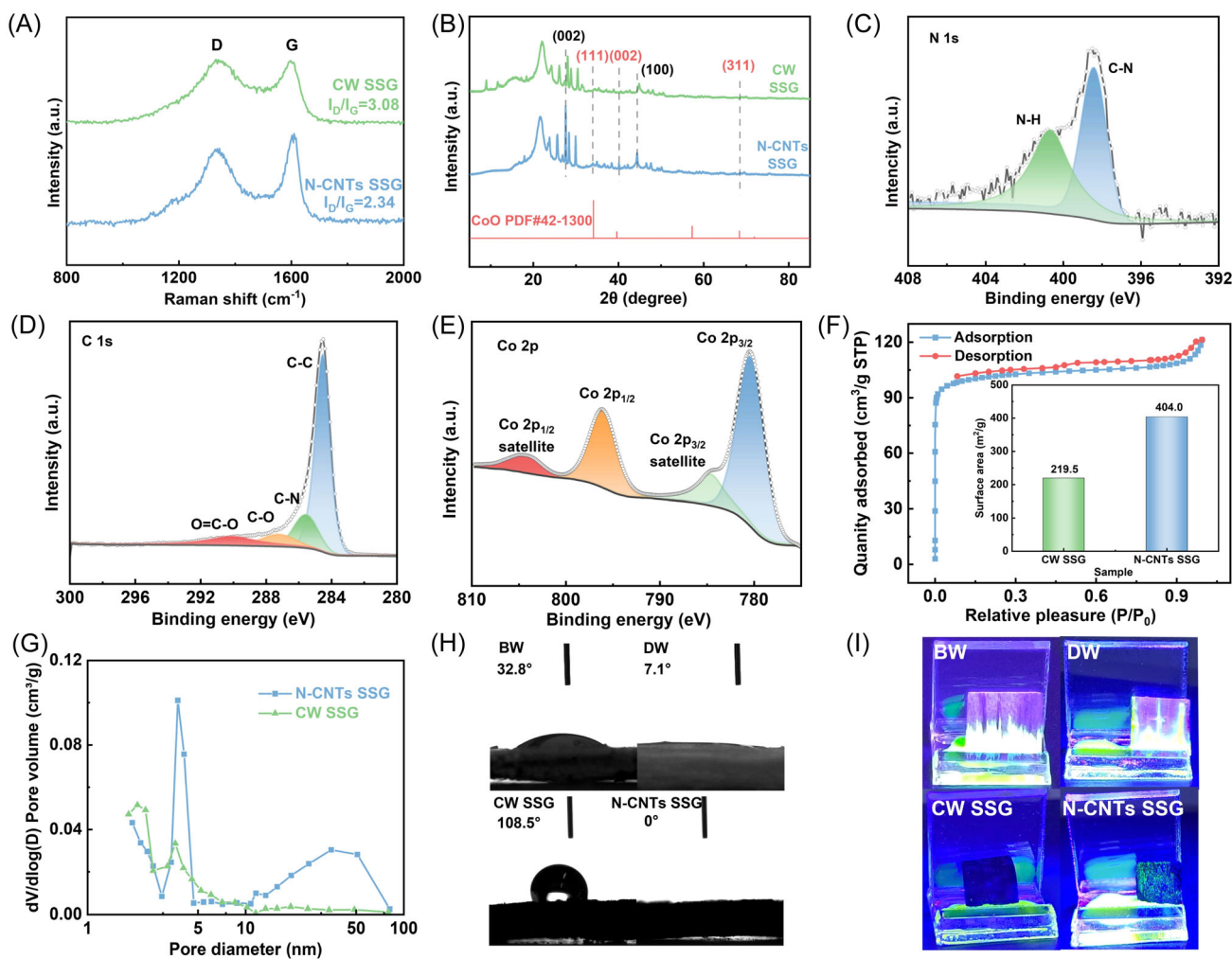


FIGURE 3 Chemical composition, porous structure, and hydrophilicity of the intestinal villi-like N-CNTs SSG and CW SSG. (A) Raman spectra of intestinal villi-like N-CNTs SSG and CW SSG; (B) XRD patterns; (C) high-resolution XPS spectra of N 1s element; (D) high-resolution XPS spectra of C 1s element; (E) high-resolution XPS spectra of Co 2p; (F) N_2 adsorption-desorption isotherms of N-CNTs SSG and specific area of N-CNTs SSG and CW SSG; (G) pore size distributions of the N-CNTs SSG and CW SSG; (H) contact angles of BW, DW, CW, and N-CNTs SSGs; (I) water transportation test using sodium fluorescein as the indicator of BW, DW, CW, and N-CNTs SSGs.

displays two types of N species, corresponding to the C–N and N–H bonds. Generally, doping N atoms in CNTs can improve the light-absorbing properties of CNTs, thus increasing the efficiency of photothermal conversion. In the high-resolution Co 2p spectrum (Figure 3E), the Co 2p_{3/2} peak, locating at 780.4 eV and corresponding to Co²⁺, further provides evidence for the presence of cobalt oxides in CNT tips.

Moreover, the in-situ growing of the intestinal villi-like N-CNTs matrices enables a much higher Brunauer Emmett-Teller (BET) surface area of 404.0 m²/g, achieving a 84.1% improvement (Figure 3F) compared with the conventional CW structure with 219.4 m²/g due to its 3D hierarchically porous structure. The pore size distributions of intestinal villi-like N-CNTs matrices (Figure 3G) demonstrate the dominance of both micropores and mesopores, confirming the hierarchically porous morphology. The mesopores mainly result from the intestinal villi-like N-CNTs matrices, and the micropores result from the defects during the growth and entanglement of N-CNTs. The low reaction temperature for CNTs results in a low degree of graphitization of the CNTs, leading to the generation of hydrophilic functional groups, such as –OH and –NH₂, on the CNT backbone. Thus, the N-CNTs SSG demonstrates outstanding superhydrophilicity (Figures 3H and S10 and Movie S1). Compared with the contact angle of 108.5° for conventional CW SSG, the contact angle is rapidly reduced to around 0° for the intestinal villi-like N-CNTs SSG within just 1 s. Further water transportation tests (Figures 3I and S11) demonstrate that intestinal villi-like N-CNTs SSG achieves excellent water transportation ability at the speed of over 0.3 cm/s. Sodium fluorescein was selected as the indicator due to the high light absorption property of the CW structure.

2.2 | Atomistic mechanism of N-CNTs in excellent solar absorptivity

Due to the quasi-blackbody feature of N-CNTs and multi-reflection of light in the 3D hierarchical CNT matrices, the intestinal villi-like N-CNTs SSG demonstrates ultrahigh solar absorptivity in the full solar spectrum, from 200 to 2400 nm. The ultraviolet-visible-near-infrared (UV-Vis-NIR) spectroscopy results (Figure 4A) demonstrate that the average absorptivity of intestinal villi-like N-CNTs SSG could be as high as 98.5%, especially at visible region and near-infrared region, which accounts for the majority of the solar energy. Although a slight decrease in solar absorptivity is observed as the wavelength increases,

the solar absorptivity at $\lambda_{\text{wave}} \geq 1800\text{ nm}$ is still higher than 95.0%, and it only accounts for less than 7.0% of the total solar energy.⁵³ Compared with the CW SSG, over 25.0% enhancement in absorptivity could be achieved (Figure 4B).

To further investigate the underlying mechanism of ultrahigh light absorption feature for the N-CNTs matrices, the AIMD calculations are performed using the density functional theory (DFT) method with the Perdew-Burke-Ernzerhof generalized gradient approximation (PBE-GGA) as the exchange-correlation function (XC).^{54–56} Two different CNT models, (4, 4) and (8, 0), are built, as shown in Figure 4C,D. A total of 64 carbon atoms are built for each of the two different configurations of the carbon nanotubes. To further investigate the N doping on the optical performance of carbon nanotubes, one, two, and three N atoms are doped in each configuration of carbon nanotubes (Figure 4C,D). The detailed model development and computational methods are given in Section 4 and Note S1.

The electric band structures and density of states (DOS) of different pristine CNT models, (4, 4) and (8, 0), at zero pressure and temperature along the high symmetry path of the Brillouin zone are demonstrated in Figures 4E,G and S12A,B. To understand the electronic properties of the N atoms interacting with the carbon nanotubes, the electric band structures with high symmetry $\Gamma \rightarrow Z$ and DOS of the N-CNTs are presented in Figures 4F,H and S12C,D. The imaginary parts, which are calculated from the electronic structure through the joint DOS and the momentum matrix elements between the occupied and the unoccupied wave functions within the selection rules, of the pristine carbon nanotubes and N-CNTs are given in Figure 4I. From the band structures and DOS result, it is evident that N-CNTs exhibit a greater number of electronic states in close proximity to the Fermi level when compared to pristine carbon nanotubes (Figures 4E–H and S12 and Table S2). The presence of a significantly larger quantity of electronic states expands the range of wavelengths absorbed by solar radiation and facilitates efficient optical transitions due to the higher DOS.

To further elucidate the effect of N doping on the optical property of carbon nanotubes, the absorption coefficient, extinction coefficient, and optical reflectivity of carbon nanotubes are calculated based on the complex dielectric constant (Figures 4J–L and S13–S15). Obviously, N-CNTs demonstrate much superior absorption performance to the pristine carbon nanotubes, especially in the visible region and near-infrared region, which account for the majority of the solar energy (Figures 4J and S13). Furthermore,

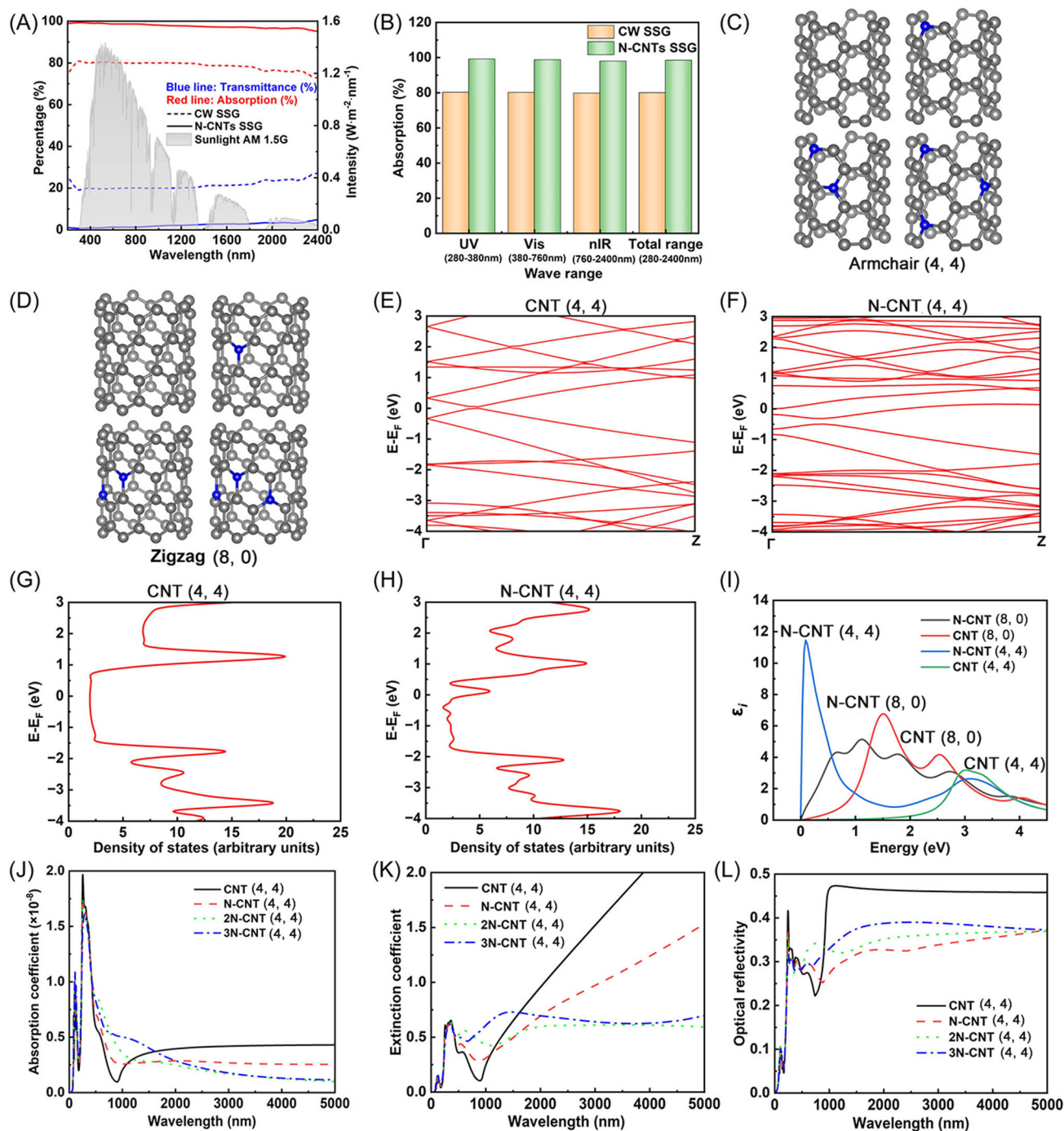


FIGURE 4 Electronic band structures, density of states (DOS), and optical spectra of the N-CNTs and pristine CNTs.

(A) Measured absorption and transmittance spectra of CW SSG and N-CNTs SSG; (B) measured absorption of the CW SSG and N-CNTs SSG in ultraviolet, visible, and near-infrared regions, respectively; (C) geometrical configurations of pristine CNTs and N-CNTs (4, 4); (D) geometrical configurations of pristine CNTs and zigzag N-CNTs (8, 0); (E, G) electronic band structures and DOS of pristine armchair CNTs; (F, H) electronic band structures and DOS of N-CNTs; (I) the imaginary parts of the N-CNTs and pristine CNTs; (J, K, L) the absorption coefficient, extinction coefficient, and optical reflectivity of armchair N-CNTs and pristine CNTs.

the absorption coefficient increases noticeably with the number of doped N atoms. Figure 4K presents the extinction coefficient of the N-CNTs. As for the armchair CNT model (4, 4), the doping of N atoms yields a

positive effect on the extinction coefficient, especially in the visible region and near-infrared region. The extinction coefficient also increased with the number of doped N atoms. Similar results are observed for

zigzag CNTs (Figure S14). Figures 4L and S15 demonstrate the optical reflectivity of the N-CNTs and pristine CNTs. It is obviously found that for armchair CNTs (4, 4), the doped N atoms achieved a noticeable decrease of optical reflectivity at $\lambda_{\text{wave}} \geq 1000\text{nm}$ compared to pristine CNTs. However, a further increase in the doped N atoms would lead to an increase in the optical reflectivity, which deteriorates the overall photothermal conversion efficiency. In conclusion, N-CNTs exhibit much superior optical performance to pristine CNTs, especially in the visible region and near-infrared region, where the photons are more easily converted into heat after absorption.

2.3 | Water production performance of intestinal villi-like N-CNTs SSG

The UV-Vis-NIR test and AIMD calculations prove excellent photothermal conversion features of the N-CNTs SSG. Then, we perform the indoor photothermal conversion and solar steam generation experiment using a solar simulator (CME-Sol8100-3A; Microenerg Technology Co., Ltd) with various illumination intensities. The illumination intensity ranges from 0.7 to 1.3 sun ($1\text{ sun} = 96\text{ mW/cm}^2$, AM1.5 G). The details about the indoor experiments can be found in Methods. Figure 5A presents the real photograph of the solar steam generation experiment. To investigate the photothermal response performance and stability of the intestinal villi-like N-CNTs SSG, the cyclic photothermal conversion experiment is conducted. The temperature curves with illumination on and off at different illumination intensities are demonstrated in Figures 5B and S16. A sharp temperature rise is observed once the illumination is switched on, indicating a perfect photothermal conversion response-ability. The rates of the temperature change (Figures 5C and S17) under different illumination intensities indicate that the intestinal villi-like N-CNTs SSG achieves a much superior photothermal conversion response rate (more than 4°C/s under one sun) to the conventional CW SSG ($<3^\circ\text{C/s}$). Moreover, the equilibrium temperature stays almost constant after the cyclic tests, proving excellent photothermal conversion stability. As shown in Figure 5D, the equilibrium temperature almost increases linearly with the illumination intensities, and the temperature difference between the intestinal villi-like N-CNTs SSG and CW SSG also increases with the illumination intensities, which indicates that the villi-like N-CNTs achieve better optical performance at high illumination intensities. The IR images of the intestinal villi-

like N-CNTs SSG and CW SSG are presented in Figures 5E, S18, and S19. Noticeably, the temperature of intestinal villi-like N-CNTs SSG could increase rapidly from 30°C to over 75°C within just 120 s.

To exactly evaluate the interfacial evaporation driven by solar energy, the evaporation experiments of pure water, CW SSG, and intestinal villi-like N-CNTs SSG under dark conditions are performed first. The foam with countersunk holes is used to support the samples (Figure 5A). To reduce the evaporation on the foam surface, bright tin foil is used to wrap the beaker so that only the surface of the sample is exposed to solar illumination. Moreover, vapor might also escape from the narrow gap between the foam and the beaker, which should also be subtracted. The quantitative weight losses of water in intestinal villi-like N-CNTs SSG, CW SSG, and the blank surface under dark conditions and various illumination intensities (from 0.7 sun to 1.3 sun) are demonstrated in Figures 5F and S20. The blank case was conducted with sealed countersunk holes to obtain the vapor loss from the narrow gap between the foam and the beaker. It is clearly observed that due to the excellent photothermal conversion efficiency, super-hydrophilicity, sufficient evaporation spots, and thermal insulation, the intestinal villi-like N-CNTs SSG demonstrates much superior evaporation performance to the conventional CW SSG. Figure 5G,H presents the variation of evaporation rate and efficiency of CW SSG and N-CNTs SSG under different illumination intensities. The solar evaporation efficiency of intestinal villi-like N-CNTs SSG is around 96.8%, approaching the thermodynamic limit, while it is just around 60% of conventional CW SSG under 1.0 sun (Figure S21). The detailed calculation process of the solar evaporation efficiency is given in Note S2. Furthermore, a linear relationship between the evaporation rate and illumination intensity is observed for intestinal villi-like N-CNTs SSG (Figure 5H), indicating that N-CNTs SSG could achieve high photothermal conversion efficiency even under strong illumination intensities. The overall performance of the present intestinal villi-like N-CNTs SSG is carefully evaluated based on the critical parameters, net solar evaporation rate and solar evaporation efficiency, under 1.0 sun (Figure 5I). Our intestinal villi-like N-CNTs SSG exhibits one of the highest solar evaporation efficiencies, surpassing state-of-the-art previously reported wood-based evaporators and non-gel evaporators (Table S3). It is noteworthy that only the net solar evaporation rate is considered, which refers to the evaporation of the solar steam generator only driven by solar energy.

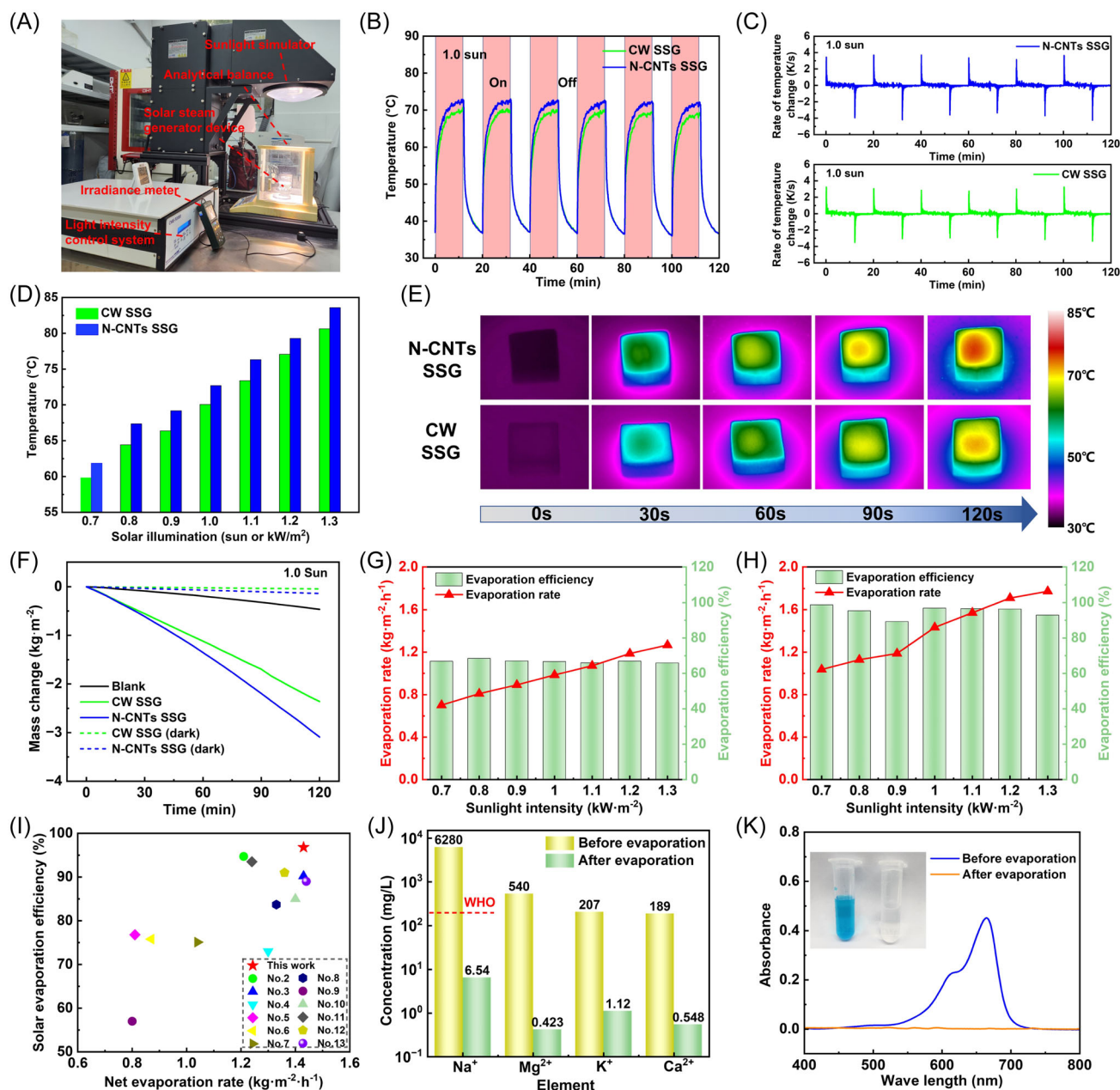


FIGURE 5 Solar evaporation performance in a laboratory environment. (A) Schematic diagram of the solar steam generator; (B) temperature variations of the intestinal villi-like N-CNTs SSG and CW SSG under on-and-off illumination mode; (C) temperature changing rates of the N-CNTs SSG and CW SSG under on-and-off illumination mode; (D) the equilibrium temperature of the intestinal villi-like N-CNTs SSG and CW SSG under different illumination intensities; (E) the IR images of the intestinal villi-like N-CNTs SSG and CW SSG under 1.0 sun irradiation; (F) the mass change of the intestinal villi-like N-CNTs SSG, CW SSG, and pure water over time under one sun irradiation; (G, H) evaporation rate and efficiency of the intestinal villi-like CW SSG and N-CNTs SSG; (I) a comparison of the solar evaporation efficiency of the intestinal villi-like N-CNTs SSG with the wood-based SSGs and non-gel SSGs. A complete list of the results reported in this graph is given in Table S3. (J) The measured concentrations of Na^+ , Mg^{2+} , K^+ , and Ca^{2+} in real seawater before and after desalination. The red dashed line represents the WHO standard. (K) The sewage treatment performance of intestinal villi-like N-CNTs SSG.

To evaluate the desalination performance of the intestinal villi-like N-CNTs SSG, the ion concentrations of Na^+ , Mg^{2+} , K^+ , and Ca^{2+} of the real seawater and the collected distilled water from N-CNTs SSG are tested (Figure 5J). The Na^+ concentration of the collected distilled water is just 1%

of the real seawater, much lower than the standard by the World Health Organization (WHO). The optical photographs of the N-CNTs SSG before and after the 20-h evaporation (Figure S22) prove the excellent salt-resistance property since no salting-out phenomenon is observed in

the used SSG. Furthermore, the sewage treatment ability of the intestinal villi-like N-CNTs SSG is evaluated using methylene blue as a pollutant. The UV-Vis-NIR absorbance spectra of the polluted water and collected distilled water from evaporation indicate that the polluted water demonstrated a strong absorption peak in the wavelength of 650 nm, which is almost eliminated in the collected water (Figure 5K). Meanwhile, the collected water turns completely colorless compared with the blue color of the raw polluted water, indicating that N-CNTs SSG achieves excellent sewage treatment ability.

To further theoretically investigate the photothermal-conversion process and evaporation performance, a theoretical model using COMSOL Multiphysics of the solar evaporation for N-CNTs SSG is developed. The detailed models and boundary conditions are given in Section 4 and Note S3. The diagram of the simulation geometry model is given in Figure S23. First, the theoretical model is validated by the measured data for N-CNTs SSG and CW SSG under different illumination intensities (Figure S24). The experimental data are measured using high-precision thermocouples in the middle of the SSGs. All the calculated temperatures agree well with the measured data, validating the reliability of the theoretical model. Furthermore, to evaluate the photothermal response ability of the theoretical model, the temperature variations of the intestinal villi-like N-CNTs SSG and CW SSG under on-and-off illumination mode are simulated and compared with the measured temperature from Figure 5B. It is clearly observed that under on-and-off illumination mode, the simulated temperature agrees well with the measured data, indicating outstanding photothermal response-ability (Figure. S25). The dynamic temperature variation under on-and-off illumination mode is given in Movie S2.

The simulations of CW SSG and intestinal villi-like N-CNTs SSG are performed with and without water. Figures 6A,B, S26, and S27 present the calculated temperature rise of the CW SSG and N-CNTs SSG without water under different illumination intensities. The temperature increases rapidly with the illumination time. As for intestinal villi-like N-CNTs SSG, its top surface temperature could increase to over 70°C rapidly, indicating excellent photothermal conversion ability. The dynamic temperature variations of CW SSG and intestinal villi-like N-CNTs SSG without water are given in Movies S3 and S4. Furthermore, after 10-min illumination, the top surface temperature of N-CNTs SSG reaches as high as 73.5°C (Figure 6E), while the bottom surface temperature is just 30°C, demonstrating excellent thermal insulation performance. The thermal conductivity test of the samples after filling with water indicated that the thermal conductivity in the axial direction (parallel to the channel direction) was 0.552 W/m/K and the radial thermal conductivity was 0.027 W/m/K. The low

thermal conductivity was attributed to the porous structure and amorphous carbon of the skeleton, which could significantly reduce the heat loss to the bulk water and surroundings. Figures 6C,D, S28, and S29 present the calculated temperature rise of the CW SSG and intestinal villi-like N-CNTs SSG with water under different illumination intensities. Compared with the temperature without water, the top surface temperature of intestinal villi-like N-CNTs SSG with water was 46.7°C (Figure 6E), while the bottom surface temperature was just 32.6°C. Most of the absorbed solar energy is used to actuate the water evaporation process. The dynamic temperature variations of CW SSG and intestinal villi-like N-CNTs SSG with water are given in Movies S5 and S6.

Based on the atomistic calculation, theoretical simulation, and indoor test, to further evaluate the working performance of the intestinal villi-like N-CNTs SSG under real outdoor circumstances, we performed the outdoor solar evaporation experiments, as depicted in Figure 6F. The intestinal villi-like N-CNTs SSG is placed on the rooftop of the Shaw Engineering Building at South China University of Technology (SCUT) with an average temperature of 31.2°C and relative humidity of 46.7% (Figure S30). The details about the outdoor solar evaporation experiments are given in Methods. The cumulative incident solar energy over the experimental period amounted to 11.58 MJ/m² (Figure S31). The mass changes of the pure water, CW SSG, and intestinal villi-like N-CNTs SSG under real solar illumination are demonstrated in Figure 6G. The real-time solar evaporation rate and efficiency indicate that the intestinal villi-like N-CNTs SSG demonstrated much superior performance to the conventional CW SSG (Figure 6H). The overall solar evaporation efficiency approaches 99.8%, much higher than that of conventional CW SSG and pure water (Figure 6I). The vapor condensation on the glass wall also confirms stronger solar evaporation performance in intestinal villi-like N-CNTs SSG (Figure S32). Further analysis indicates that even in late afternoon (3–4 p.m.) with weak solar illumination intensity and high solar altitude angle, the solar evaporation efficiency remained almost constant, confirming the exceptional solar energy-harvesting capacity demonstrated by the intestinal villi-like N-CNTs SSG at high solar altitude angles. It is mainly attributed to the multi-reflection and diffuse reflection by the villi-like N-CNTs (Figure 6J). Thus, our intestinal villi-like N-CNTs SSG demonstrates great potential in photothermal conversion under all-day and all-season circumstances, especially in the late afternoon and winter with low incidence angles.

To further evaluate the evaporation performance of the intestinal villi-like N-CNTs SSG in high salt concentration applications, real seawater and high-salinity brine were used. Table S4 presents the concentration of

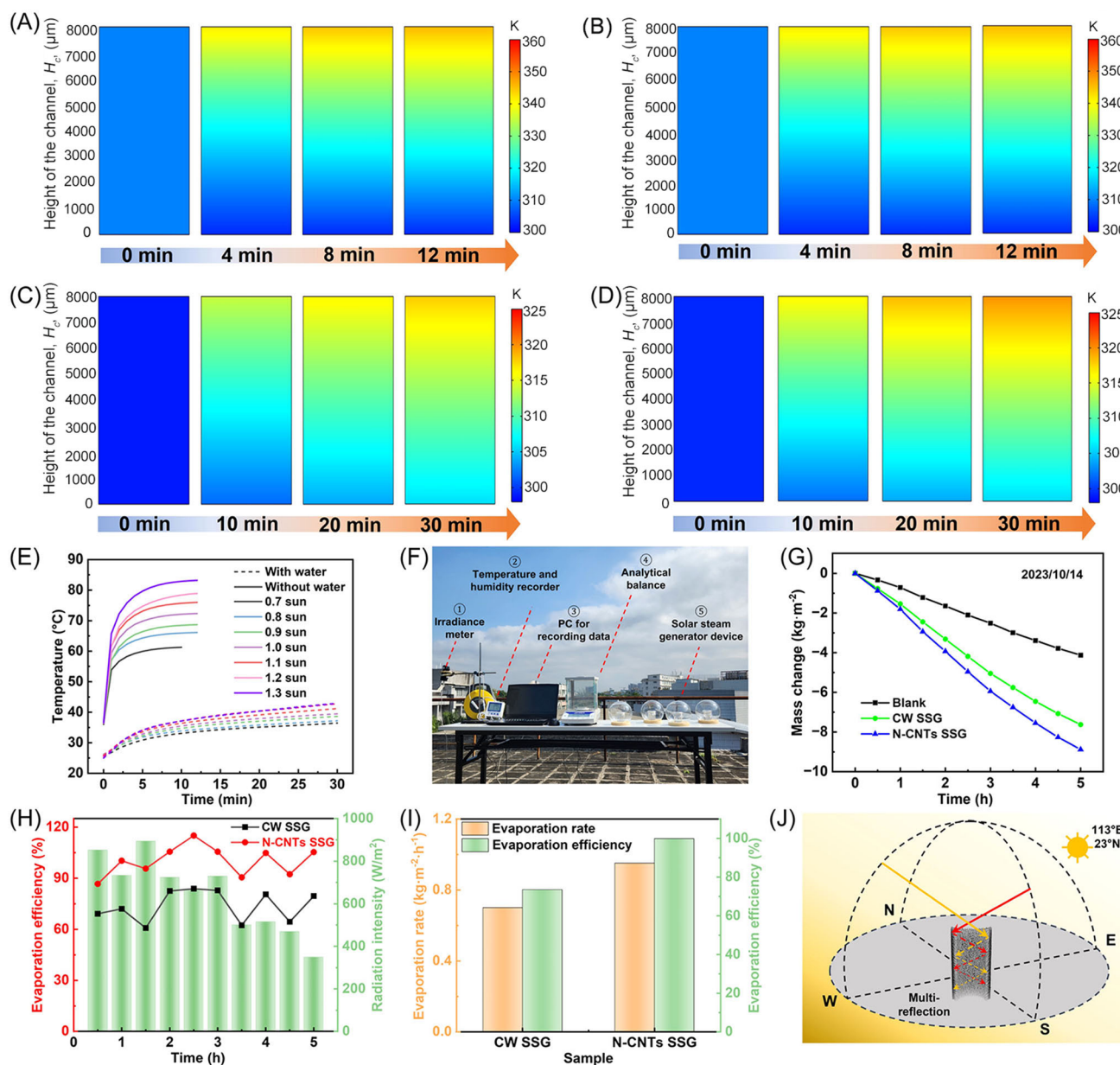


FIGURE 6 Simulation solar evaporation process and outdoor experiments of the intestinal villi-like N-CNTs SSG and CW SSG. Temperature variations of conventional CW SSG and intestinal villi-like N-CNTs SSG (A, B) without water and (C, D) with water in the full domain; (E) variation of the top surface temperature in the intestinal villi-like N-CNTs SSG; (F) photograph of the outdoor solar evaporation experiments; (G) the mass change of the intestinal villi-like N-CNTs SSG, CW SSG, and pure water over time under practical irradiation; (H, I) evaporation rate and efficiency of the intestinal villi-like N-CNTs SSG and CW SSG; (J) sunlight illumination on the intestinal villi-like N-CNTs SSG from different directions. Both the zenith angle and altitude angle are considered.

each solute in simulated seawater. The evaporation test showed that, in simulated seawater application, the net evaporation rate was $1.439 \text{ kg/m}^2/\text{h}$ with an evaporation efficiency of 97.21% (Figure S33 and Table S5). However, as the concentration increased to 10%, the net evaporation rate was reduced to $1.106 \text{ kg/m}^2/\text{h}$. The decrease was mainly attributed to the accumulation of salt, which could prevent the effect of water transportation in the vertically aligned channels.

3 | DISCUSSION

To illustrate the atomistic mechanism of N doping on the photothermal conversion performance in CNTs, we performed the AIMD simulations. The molecular simulation results clearly reveal why N-CNTs exhibit much superior optical performance to the pristine CNTs. The results indicate that N-CNTs exhibit a greater number of electronic states in close proximity to the Fermi level when

compared to pristine CNTs (Figures 4E–H and S12). The presence of a significantly larger quantity of electronic states expands the range of wavelengths absorbed by solar radiation and facilitates efficient optical transitions due to the high DOS.

The overall high efficiency of the solar steam generator is attributed to three aspects, which are consistent with the typical three steps in the solar evaporation process, namely water transportation, phase transition, and vapor diffusion. According to the cascade theory, each step should be strengthened if we want to intensify the overall evaporation performance. Our intestinal villi-like N-CNTs SSG successfully intensifies the evaporation process via these steps. First, due to the excellent hydrophilicity of the N-CNTs matrices and the capillary effect of the vertically aligned channels, the N-CNTs SSG demonstrates outstanding superhydrophilicity and excellent water transportation ability at the speed of over 0.3 cm/s (Figures 3H,I, S10, and S11), which ensures a sufficient water supply. Second, the ultrahigh photothermal conversion property with the full solar spectrum of the N-CNT matrices and multi-reflection and diffuse reflection in the channels could provide enough heat for the phase transition (Figure 3A). Furthermore, the huge increase in the specific surface area intensifies the interface between solid structure and liquid water and offers sufficient evaporation spots (Figure 3F). Third, the 3D vertically aligned microchannels and interconnected pore networks also provide a rapid routine for vapor escape and avoid vapor accumulation (Figure 2B,C). Apart from these three steps, the overall solar evaporation performance is also influenced by the heat loss from the photothermal conversion interface to the bulk water. Benefiting from the porous structure and extremely low thermal conductivity of the amorphous carbon skeleton, our intestinal villi-like N-CNTs SSG demonstrates excellent thermal insulation ability and significantly reduces the heat loss from the localized heat surface to the bulk water (Figure 6A–D).

In summary, inspired by human intestinal villi structure, we designed and fabricated a novel intestinal villi-like N-CNTs SSG, consisting of 3D hierarchical CNT matrices, to achieve ultrahigh photothermal conversion and solar evaporation efficiencies. The solar evaporation efficiency is as high as 96.8%. The novel intestinal villi-like N-CNTs SSG also demonstrates outstanding desalination performance and salt-resistance properties. Furthermore, benefiting from the excellent photothermal conversion property with full solar spectrum of the N-CNTs matrices and multi-reflection and diffuse reflection in the vertically aligned channels, our intestinal villi-like N-CNTs SSG has great potential in all-day and all-season solar energy applications.

4 | METHODS

4.1 | AIMD calculations

The AIMD calculations of the N-CNTs were performed using the DFT method with the PBE-GGA as the XC.^{47–49} The plane wave pseudopotential and ultrasoft pseudopotential methods were employed using Quantum Espresso software version 7.2.⁵⁷ The plane wave cutoff energy was set to 90 Rydberg, and a 10 Å vacuum was used to separate periodic copies in the *x* and *y* directions. Total energy convergence was achieved with a $1 \times 1 \times 15$ Monkhorst-Pack *k*-point sampling until the force on each atom was less than 0.01 eV/Å. Non-self-consistent field (NSCF) and DOS calculations were performed using a $2 \times 2 \times 30$ Monkhorst-Pack *k*-point grid.

4.2 | Fabrication of CW SSG

A 3D scaffold with vertically aligned channels was obtained through delignification and carbonization of balsa wood. Balsa wood was picked out among various candidate materials, such as poplar wood, paulownia wood, linden wood, white oak wood, pine wood, pear wood, and balsa wood. First, the balsa wood was cut into blocks with the dimension of $20 \times 20 \times 10 \text{ cm}^3$, vertically to the growth direction. Then, the blocks were immersed in aqueous 1 w.t.% NaClO₂ solution at 80°C for 8 h to remove lignin. The pH of the solution was adjusted to 4.0 using acetic acid. Then, the delignified blocks were boiled in deionized water for 15 min, and above procedure was repeated several times until the greenish-yellow rinsing water turned colorless. After that, the delignified wood (DW) was freeze-dried at –40°C for 24 h. Finally, the DW was carbonized using a tube furnace at 700°C in an argon atmosphere for 120 min to obtain the CW SSG.

4.3 | Fabrication of intestinal villi-like N-CNTs SSG

The N-CNTs SSG was prepared via T-CVD technology for in-situ growing N-doped CNTs on the carbonized vertically aligned channels. The prepared CW SSG was immersed in a 3 w.t.% Co(NO₃)₂ solution for 24 h and then transferred and stirred in 0.2 mol/L NaOH solution for 20 min at 25°C. The synthesized Co(OH)₂ was loaded in the channel surface and acted as the precursor for in-situ growing of N-CNTs. The C₃H₆N₆ (melamine), as a carbon source, was placed in a ceramic boat and loaded into the center of the reactor. The N-CNT fibers successfully grew on the surface of the vertically aligned channels at 700°C for 120 min in an argon

atmosphere. The height and distribution of the in-situ N-CNTs fibers can be controlled by varying the growth time.

4.4 | Indoor solar evaporation experiments

The indoor evaporation performances of the intestinal villi-like N-CNTs SSG and CW SSG were measured using a solar simulator (CME-Sol8100-3A; Microenerg Technology Co., Ltd) as the simulated solar source. The illumination intensity ranged from 0.7 sun to 1.3 sun (1 sun = 96 mW/cm², AM1.5 G). The experimental setup is shown in Figure 5A. The SSGs were floated on the water surface, supported by polystyrene foam. Before each test, the intensity of light was calibrated using a photodiode. The room temperature and relative humidity were controlled around 25°C and 45%, respectively. The mass change of intestinal villi-like N-CNTs SSG and CW SSG was recorded continuously using an electronic balance (GL2202L-1SCN; Sartorius). The temperature variations of the N-CNTs SSG and CW SSG were recorded by a thermal infrared camera (A6702sc; FLIR). The evaporation rate under dark conditions at the same temperature and humidity was also measured and used to calibrate the SSG data.

4.5 | Outdoor solar evaporation experiments

The outdoor evaporation of the N-CNTs SSG and CW SSG was performed in Guangzhou, China on October 14, 2023. The experimental setup is shown in Figure 6F. The solar intensity was recorded continuously by a solar irradiance meter (TES-1333R; TES Electrical Electronic Corp.). The ambient temperature and humidity were measured by a temperature and humidity sensor (SCP110; Schneider Electric). The mass change of N-CNTs SSG and CW SSG was also recorded continuously using an electronic balance (GL2202L-1SCN; Sartorius).

4.6 | Materials characterizations

The microstructures and element distribution of the SSGs were obtained using SEM (SU8220; HITACHI) and transmission electron microscope (JEM-2100F; JEOL). The electrical transport properties of functional groups were characterized by Raman spectroscopy (LabRAM Aramis; Horiba Jobin Yvon) and XPS (Axis Supra+; Kratos). The crystalline structure was characterized by XRD (Miniflex 600; Rigaku) with a scanning

rate of 5°/min. The light transmittance and reflectance spectra were measured by a UV-visible-near-IR spectrometer (Lambda950; PerkinElmer). The specific surface area and pore properties of the SSGs were measured using the BET method (ASAP2460; Micromeritics). The contact angle of SSGs was measured at room temperature (~25°C) by a contact angle meter (OCA25; DataPhysics) using a 5 mL water droplet. The water-pumping ability of the SSGs was measured through the dipping test using fluorescein sodium as the indicator.

4.7 | Modeling for solar evaporation of intestinal villi-like N-CNTs SSG and CW SSG

The photothermal conversion process and temperature distribution in the intestinal villi-like N-CNTs SSG and CW SSG were simulated using COMSOL Multiphysics. The radiative transfer equation (RTE) was employed to describe the process of spectral attenuation of radiation within the medias.⁵⁸

$$\Omega \cdot \nabla I(\Omega) = \kappa_{\text{nf}} I_b(T) - \beta_{\text{nf}} I(\Omega) + \frac{\sigma_{\text{s,nf}}}{4\pi} \int_0^{4\pi} I(\Omega') \phi(\Omega', \Omega) d\Omega', \quad (1)$$

where $I(\Omega)$ is the radiative intensity at a given position following the Ω direction, W/(m² sr). κ_{nf} , β_{nf} , and $\sigma_{\text{s,nf}}$ are the absorption, extinction, and scattering coefficients of the media, respectively. $\phi(\Omega', \Omega)$ is the scattering phase function. $I_b(T)$ is the blackbody radiative intensity, W/(m² sr). Considering the conservation of the incident radiation, the heat flux divergence is given as follows:

$$\nabla \cdot q_r = \frac{\partial q_r}{\partial y} = \kappa_{\text{nf}} [G - 4\pi I_b(T)]. \quad (2)$$

The incident radiation is considered an internal heat source and the energy conservation equation of the fluid part is given as follows:

$$\rho_f C_p \frac{\partial T}{\partial t} = k_f \left(\frac{\partial^2 T}{\partial x^2} + \frac{\partial^2 T}{\partial y^2} \right) - \frac{\partial q_r}{\partial y}. \quad (3)$$

The detailed boundary conditions are presented in Note S3.

AUTHOR CONTRIBUTIONS

Chuanshuai Dong and Lei Chen conceived the idea and performed the experiments. Weiquan Lin and Huan Liu

performed the outdoor experiments. Lizhi Zhang and Chaohua Peng performed the theoretical calculation. Lin Lu and Ronghui Qi conducted the theoretical analysis. Chuanshuai Dong and Lizhi Zhang co-wrote the manuscript. All the authors discussed the results and approved the final version of the manuscript.

ACKNOWLEDGMENTS

The project is supported by the National Natural Science Foundation of China (NSFC) (Nos. 52476072 and 51936005), Guangdong Basic and Applied Basic Research Foundation (No. 2024A1515030035), Guangdong Provincial University Innovation Team Project (No. 2023KCXTD038), and Key Laboratory of Advanced Reactor Engineering and Safety of Ministry of Education.

CONFLICT OF INTEREST STATEMENT

The authors declare that there are no conflicts of interests.

DATA AVAILABILITY STATEMENT

The authors declare that the data supporting the findings of this study are available within the paper and its Supporting Information files.

ORCID

Chuanshuai Dong  <http://orcid.org/0000-0002-7905-7637>

Lin Lu  <http://orcid.org/0000-0002-4114-3468>

REFERENCES

- Xu N, Li J, Finnerty C, et al. Going beyond efficiency for solar evaporation. *Nat Water*. 2023;1(6):494-501.
- Zhang Y, Tan SC. Best practices for solar water production technologies. *Nat Sustain*. 2022;5(7):554-556.
- Wang Z, Horseman T, Straub AP, et al. Pathways and challenges for efficient solar-thermal desalination. *Sci Adv*. 2019;5(7):eaax0763.
- Liu S, Huang C, Huang Q, Wang F, Guo C. A new carbon-black/cellulose sponge system with water supplied by injection for enhancing solar vapor generation. *J Mater Chem A*. 2019;7(30):17954-17965.
- Liang H, Liao Q, Chen N, et al. Thermal efficiency of solar steam generation approaching 100% through capillary water transport. *Angew Chem Int Ed*. 2019;131(52):19217-19222.
- Wang X, Lin Z, Gao J, et al. Solar steam-driven membrane filtration for high flux water purification. *Nat Water*. 2023;1(4):391-398.
- Gao J, Zhang L, You J, et al. Extreme salt-resisting multistage solar distillation with thermohaline convection. *Joule*. 2023;7(10):2274-2290.
- Xu Z, Yu J, Shan H, et al. Solar evaporation with solute replacement towards real-world applications. *Energy Environ Sci*. 2023;16(11):5325-5338.
- Yu Z, Gu R, Tian Y, Xie P, Jin B, Cheng S. Enhanced interfacial solar evaporation through formation of micro-menisciuses and microdroplets to reduce evaporation enthalpy. *Adv Funct Mater*. 2022;32(17):2108586.
- Zhou L, Tan Y, Wang J, et al. 3D self-assembly of aluminium nanoparticles for plasmon-enhanced solar desalination. *Nat Photonics*. 2016;10(6):393-398.
- brahim I, Seo DH, Angeloski A, McDonagh A, Shon HK, Tijing LD. 3D microflowers CuS/Sn₂S₃ heterostructure for highly efficient solar steam generation and water purification. *Sol Energy Mater Sol Cells*. 2021;232:111377.
- Li X, Tian Y, Zhang P, et al. A Lotus-petiole-inspired hierarchical design with hydrophilic/hydrophobic management for enhanced solar water purification. *Adv Funct Mater*. 2023;33(31):2302019.
- Meera B, Vidhya C, Nair RB, Surya R, Kurian S. Sustainable sponge-like composite hydrogel evaporator for highly efficient solar steam generation. *Mater Today Sustain*. 2023;23:100439.
- Poredoš P, Wang R. Sustainable cooling with water generation. *Science*. 2023;380(6644):458-459.
- Fu J, Li Z, Li X, et al. Hierarchical porous metallic glass with strong broadband absorption and photothermal conversion performance for solar steam generation. *Nano Energy*. 2023;106:108019.
- Ni G, Li G, Boriskina SV, et al. Steam generation under one sun enabled by a floating structure with thermal concentration. *Nat Energy*. 2016;1(9):16126.
- Nepal D, Kang S, Adstedt KM, et al. Hierarchically structured bioinspired nanocomposites. *Nat Mater*. 2023;22(1):18-35.
- Wang F, Lee J, Chen L, et al. Inspired by wood: thick electrodes for supercapacitors. *ACS Nano*. 2023;17(10):8866-8898.
- Chen C, Kuang Y, Zhu S, et al. Structure-property-function relationships of natural and engineered wood. *Nat Rev Mater*. 2020;5(9):642-666.
- Wu L, Dong Z, Cai Z, et al. Highly efficient three-dimensional solar evaporator for high salinity desalination by localized crystallization. *Nat Commun*. 2020;11(1):521.
- Xie M, Zhang P, Cao Y, Yan Y, Wang Z, Jin C. A three-dimensional antifungal wooden cone evaporator for highly efficient solar steam generation. *npj Clean Water*. 2023;6(1):12.
- Mehrkhah R, Goharshadi EK, Ghafurian MM, Mohammadi M, Mahian O. Clean water production by non-noble metal/reduced graphene oxide nanocomposite coated on wood: scalable interfacial solar steam generation and heavy metal sorption. *Sol Energy*. 2021;224:440-454.
- Cui T, Liu Z, Gao L, et al. Engineered wood with hierarchically tunable microchannels toward efficient solar vapor generation. *Langmuir*. 2022;38(42):12773-12784.
- Jia C, Li Y, Yang Z, et al. Rich mesostructures derived from natural woods for solar steam generation. *Joule*. 2017;1(3):588-599.
- Ding M, Zhao D, Feng P, et al. Highly efficient 3D solar evaporator for zero liquid discharge desalination of high-salinity brine. *Carbon Energy*. 2024;6:e548.
- Zhao D, Ding M, Lin T, et al. Gradient graphene spiral sponges for efficient solar evaporation and zero liquid discharge desalination with directional salt crystallization. *Adv Sci*. 2024;11(22):2400310.
- Ding M, Lu H, Sun Y, et al. Superelastic 3D assembled clay/graphene aerogels for continuous solar desalination and oil/organic solvent absorption. *Adv Sci*. 2022;9(36):2205202.

28. Ding M, Zhao D, Wei R, et al. Multifunctional elastomeric composites based on 3D graphene porous materials. *Exploration*. 2024;4(2):20230057.
29. Li T, Liu H, Zhao X, et al. Scalable and highly efficient mesoporous wood-based solar steam generation device: localized heat. *Adv Funct Mater*. 2018;28(16):1707134.
30. Saleque AM, Ma S, Thakur AK, et al. MXene/MnO₂ nanocomposite coated superior salt-rejecting biodegradable luffa sponge for efficient solar steam generation. *Desalination*. 2023;554:116488.
31. Wong MY, Zhu Y, Ho TC, Pan A, Tso CY. Polypyrrole-reduced graphene oxide coated delignified wood for highly efficient solar interfacial steam generation. *Appl Therm Eng*. 2023;219 (Part D):119686.
32. Setyawan H, Juliananda J, Widiyastuti W. Engineering materials to enhance light-to-heat conversion for efficient solar water purification. *Ind Eng Chem Res*. 2022;61(49):17783-17800.
33. Chen S, Sun Z, Xiang W, et al. Plasmonic wooden flower for highly efficient solar vapor generation. *Nano Energy*. 2020;76:104998.
34. Soo Joo B, Soo Kim I, Ki Han I, Ko H, Gu Kang J, Kang G. Plasmonic silicon nanowires for enhanced heat localization and interfacial solar steam generation. *Appl Surf Sci*. 2022;583: 152563.
35. Li W, Li X, Liu J, et al. Coating of wood with Fe₂O₃-decorated carbon nanotubes by one-step combustion for efficient solar steam generation. *ACS Appl Mater Interfaces*. 2021;13(19): 22845-22854.
36. Zahmatkesh BB, Niazmand H, Goharshadi EK, et al. Synergistic effect of Fe₃O₄ nanoparticles and Au nanolayer in enhancement of interfacial solar steam generation. *Mater Res Bull*. 2023;162:112178.
37. Wilson HM, Ahirrao DJ, Raheman Ar S, Jha N. Biomass-derived porous carbon for excellent low intensity solar steam generation and seawater desalination. *Sol Energy Mater Sol Cells*. 2020;215:110604.
38. Saleque AM, Ahmed S, Ivan MNAS, et al. High-temperature solar steam generation by MWCNT-HfTe₂ van der Waals heterostructure for low-cost sterilization. *Nano Energy*. 2022;94:106916.
39. Bhowmik, PK, Schlegel JP. Multicomponent gas mixture parametric CFD study of condensation heat transfer in small modular reactor system safety. *Exp Comput Multi Flo*. 2023; 5(1):15-28.
40. Suh Y, Chang S, Simadiris P, et al. VISION-iT: a framework for digitizing bubbles and droplets. *Energy AI*. 2024;15:100309.
41. Shi Y, Li R, Jin Y, et al. A 3D photothermal structure toward improved energy efficiency in solar steam generation. *Joule*. 2018;2(6):1171-1186.
42. Li X, Xu W, Tang M, et al. Graphene oxide-based efficient and scalable solar desalination under one sun with a confined 2D water path. *Proc Natl Acad Sci U S A*. 2016;113(49): 13953-13958.
43. Menon AK, Haechler I, Kaur S, Lubner S, Prasher RS. Enhanced solar evaporation using a photo-thermal umbrella for wastewater management. *Nat Sustain*. 2020;3(2):144-151.
44. Bang J, Moon IK, Oh J. Three-dimensional multimodal porous graphene-carbonized wood for highly efficient solar steam generation. *Sustainable Energy Technol Assess*. 2023;57:103199.
45. Liu S, Li S, Lin M. Understanding interfacial properties for enhanced solar evaporation devices: from geometrical to physical interfaces. *ACS Energy Lett*. 2023;8(4):1680-1687.
46. Koirala, R, Inthavong K, Date A. Numerical study of flow and direct contact condensation of entrained vapor in water jet ejector. *Exp Comput Multi Flo*. 2022;4:291-303.
47. Li X, Lin R, Ni G, et al. Three-dimensional artificial transpiration for efficient solar wastewater treatment. *Natl Sci Rev*. 2018;5(1):70-77.
48. Hertwig, T, Wittmann T, Wiśniewski P, Friedrichs J. Modeling condensing flows of humid air in transonic nozzles. *Exp Comput Multi Flo*. 2023;5(4):344-356.
49. Yang B, Zhang Z, Liu P, et al. Flatband λ -Ti₃O₅ towards extraordinary solar steam generation. *Nature*. 2023;622(7983):499-506.
50. Taylor SR, Ramsamooj S, Liang RJ, et al. Dietary fructose improves intestinal cell survival and nutrient absorption. *Nature*. 2021;597(7875):263-267.
51. Moor AE, Harnik Y, Ben-Moshe S, et al. Spatial reconstruction of single enterocytes uncovers broad zonation along the intestinal villus axis. *Cell*. 2018;175(4):1156-1167.e15.
52. Pham-Huu C, Vieira R, Louis B, et al. About the octopus-like growth mechanism of carbon nanofibers over graphite supported nickel catalyst. *J Catal*. 2006;240(2):194-202.
53. Davy NC, Sezen-Edmonds M, Gao J, et al. Pairing of near-ultraviolet solar cells with electrochromic Windows for smart management of the solar spectrum. *Nat Energy*. 2017;2(8): 17104.
54. Perdew JP, Burke K, Ernzerhof M. Generalized gradient approximation made simple. *Phys Rev Lett*. 1996;77(18): 3865-3868.
55. Kayang KW, Nyankson E, Efavi JK, et al. A comparative study of the interaction of nickel, titanium, palladium, and gold metals with single-walled carbon nanotubes: a DFT approach. *Results Phys*. 2019;12:2100-2106.
56. Adara PP, Oyinbo ST, Jen TC. Density functional theory simulation and modeling of the electrical and mechanical properties of Al₂O₃-CAO-CNT (3,3) nanomaterial. *Comput Mater Sci*. 2023;218:111939.
57. Amounas S, Hbab A, Ait Lamine L, Chaib H, Ait-Taleb T. Dependence of tetragonal barium titanate spontaneous polarization and refractive indices on DFT exchange-correlation functionals. *Phys B*. 2024;674:415536.
58. Modest, MF, Mazumder, S. *Radiative Heat Transfer*. Academic Press, 2021.

SUPPORTING INFORMATION

Additional supporting information can be found online in the Supporting Information section at the end of this article.

How to cite this article: Dong C, Chen L, Lin W, et al. Nature-inspired 3D hierarchical carbon nanotube matrices enable extraordinary solar steam generation. *Carbon Energy*. 2025;7:e655. doi:10.1002/cey2.655